Deep–Sea Research I 194 (2023) 103968

Contents lists available at ScienceDirect

Deep-Sea Research Part I

journal homepage: www.elsevier.com/locate/dsri

Multiscale energy analysis of the impact of Typhoon Kalmaegi in the South China Sea

Gang Li[a], Yijun He[a,b,*], Yang Yang[a], Guoqiang Liu[a,c,d], Xiaojie Lu[a], William Perrie[d]

[a] School of Marine Sciences, Nanjing University of Information Science and Technology, Nanjing, 210044, China
[b] Key Laboratory of Space Ocean Remote Sensing and Applications, Beijing, 100081, China
[c] Southern Marine Science and Engineering Guangdong Laboratory, Zhuhai, Guangdong, China
[d] Fisheries and Oceans Canada, Bedford Institute of Oceanography, Dartmouth, NS, B2Y 4A2, Canada

ARTICLE INFO

Keywords:
Typhoon response
Localized multiscale energy and vorticity analyses
South China Sea

ABSTRACT

We apply a localized multiscale energetics framework to study the multiscale interactions between near-inertial and mesoscale processes during the passage of Typhoon Kalmaegi in the South China Sea. The original HYCOM variable fields are decomposed into a low-frequency background flow window, a mid-frequency flow window and a high-frequency process window. Our results show that the background window represents mesoscale processes and Kuroshio currents well and the mid-frequency window captures near-inertial processes influenced by typhoon-induced wind stresses. The kinetic energy transfers from the near-inertial window to the background window, mainly on the right-hand side of the typhoon track. Advection redistributes energy, transporting kinetic energy downward from the ocean surface. Pressure work, which is stronger than advection processes, contributes to the accumulation of kinetic energy in the mid-frequency flow window and enhances ocean mixing. Negative vorticity has a significant impact on the distribution and downward propagation of the near-inertial energy, leading to heterogeneity in the mixing of the upper ocean. Negative vorticity and pressure work partially result in "leftward abnormal enhancement", the magnitude of which is smaller than the increase in the near-inertial energy. We offer new insights into understanding the multiscale interactions between typhoons and the upper ocean.

1. Introduction

Tropical cyclones (referred to as typhoons in the Pacific Ocean) have significant impacts on the sea surface temperature (SST) and the thermal structure of the upper ocean by driving ocean movements (Babin et al., 2004; Jin et al., 2020). Specifically, deepening of the mixed layer and cooling of the SST in the mixed layer result from vertical mixing and entrainment when typhoons pass over the affected regions (Yue et al., 2018). Typhoon-induced cooling of the SST affects the intensity of the typhoon as a result of negative feedback (Lin et al., 2008), which, in turn, affects the energy transferred into the storm from the ocean via evaporation and conduction (Leipper and Volgenau, 1972; Zheng et al., 2010). Cooling also transports nutrient-rich deep water into the upper ocean and enhances phytoplankton growth, increasing the primary productivity (Lin et al., 2003; Liu and Tang, 2018; Zheng et al., 2010).

The responses of the ocean are significantly affected by the characteristics of the typhoon (e.g., the wind speed, translation speed and typhoon intensity) and the pre-existing conditions in the upper ocean (e.g., mesoscale eddies and the depth of the mixed layer) (Pan et al., 2017; Zhao et al., 2017). The intensity and translation speed of the typhoon affect vertical mixing and upwelling and the wind stress directly affects Ekman pumping (Pan et al., 2018; Shan et al., 2014; Shang et al., 2008; Zhao et al., 2013). As a ubiquitous oceanic feature, mesoscale eddies have a horizontal scale of 100–500 km and an amplitude of 5–25 cm on a spatial scale of 50–200 days (Fu et al., 2010; Morrow and Le Traon, 2012). Cyclonic (anticyclonic) eddies, which are associated with internal upwelling (downwelling), enhance (suppress) the response of the ocean to typhoons as a result of the elevated (depressed) depth of the mixed layer (Sun et al., 2010). The status of the pre-existing eddies in the ocean can therefore alter the amount of cooling of the SST and the resultant chlorophyll blooms on the sea surface (Liu and Tang, 2018; Wang et al., 2016; Yue et al., 2018; Zhang et al., 2016). However, there is still a lack of statistical characterization of the multiscale transport and transfer of energy on both horizontal and vertical scales.

---

* Corresponding author. School of Marine Sciences, Nanjing University of Information Science and Technology, Nanjing, 210044, China.
E-mail address: yjhe@nuist.edu.cn (Y. He).

https://doi.org/10.1016/j.dsr.2023.103968
Received 29 October 2022; Received in revised form 14 December 2022; Accepted 13 January 2023

Interactions between eddies and typhoons have been considered as an important air–ocean process in previous studies of typhoon-induced near-inertial oscillations and wind stress curl (Jin et al., 2020; Yue et al., 2018). A diagnostic methodology of the time-varying energetics, on the basis of the multiscale window transform (MWT) —namely, localized multiscale energy and vorticity analysis (MS-EVA)—has been used in the multiscale energetic diagnosis of the response of oceans to the passage of typhoons (Chai and Wang, 2019). In the Mokpo area, the results of these studies have shown that the reconstructed large-scale, abnormal warming-scale and high-frequency tide-scale windows, can be attributed to the transfer energy, the transport of kinetic energy (KE) and wind stress, respectively. In addition, the transport of KE in the warm-scale window is enhanced when the typhoon passes over an area, whereas barotropic instabilities and a strong wind stress affect the transfer of KE. However, Chai & Wang (2019) paid more attention to the warm-scale window and horizontal changes. The interactions of the energy transfer induced by typhoons and eddies also need to be clarified.

Previous studies have suggested that the response of the ocean to typhoons and the interactions of typhoons and ocean eddies will help us to understand the changes in the ocean during the passage of typhoons. We still need to quantify the interactions between typhoons and eddies during this passage. MS-EVA could help us to understand the influence of the background flow and the flows associated with typhoons and could also contribute to studies of the multiscale processes of typhoon-induced energy exchange in the upper ocean. We revisit these issues by using MS-EVA to investigate energy transfers during the passage of Typhoon Kalmaegi (2014) in the South China Sea (SCS), which allows us to obtain the multi-aspect statistical characteristics of the ocean response to typhoons in this region.

This paper is organized as follows. The data and a brief description of MS-EVA are introduced in Section 2. Our results and verification of the use of MS-EVA to investigate typhoons are presented in Section 3. Section 4 introduces the multiscale impacts of vorticity on the near-inertial energy and Section 5 provides a summary of our results.

2. Data and methods

2.1. Data

We use the West North Pacific Ocean Best Track Data of six-hourly storm observations from the Joint Typhoon Warning Center to analyze the best-track information for Typhoon Kalmaegi (www.metoc.navy.mil/jtwc/jtwc.html?western-pacific). We carry out a diagnostic analysis of the interactions between eddy energy and typhoons via MS-EVA using Typhoon Kalmaegi (2014) as an example. The best track data in our study region (105–128° E, 10–28° N) is integrated onto a single diagram (Fig. 1). Typhoon Kalmaegi was generated at 12:00 UTC on September 12, 2014 and entered our study region at 12:00 UTC on September 13, 2014.

We use the model outputs from the Hybrid Coordinate Ocean Model with Naval Research Laboratory Coupled Ocean Data Assimilation global 1/12° reanalysis dataset (HYCOM, www.hycom.org) as the input to the MS-EVA application. The HYCOM dataset is chosen because it has been used in previous diagnostic analyses of energy cascades (Wu and Li, 2018; Yang and Liang, 2018; Quan et al., 2022). We use three-hourly outputs during the time period in which the typhoons passed through our survey region.

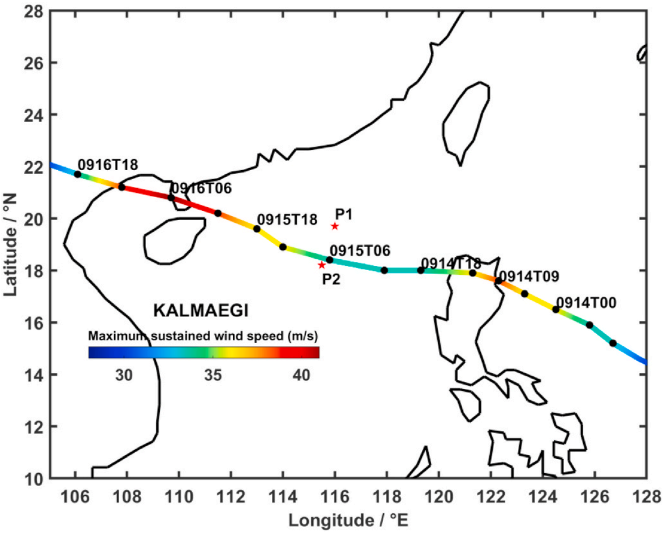

Fig. 1. The track of Typhoon Kalmaegi (2014) over our study region obtained from the Joint Typhoon Warning Center. The values on the legend indicate the maximum sustained wind speed (units: m s^{-1}). The interval between each point in the tracks is 6 h. The times at the start and end of the track are the times when the typhoon entered the study region and then dissipated, respectively. The two red stars P1 and P2 are the positions of the moorings.

Table 1
Location and water depth of two moorings.

Station	Location	Water depth	Depth intervals
P1	116.0° E, 19.7° N	1630 m	8 m intervals from 14 m to 246 m 4 m intervals from 157.76 m to 273.76 m
P2	115.5° E, 18.2° N	3840 m	16 m intervals from 304.7 m to 848.7 m

Two moorings from the coss-shaped observation array are used to reval the flow variability and evaluate HYCOM outputs. The positions of the two mooring are on either side of the track (red stars in Fig. 1). Velocity data measured by three Acoustic Doppler Current Profilers was recorded for about 4 months from June 16, 2014 to October 11, 2014 on the right side of the track (hereinafter P1) and approximately 9 months months from June 8, 2014 to March 29, 2015 on the left side (hereinafter P2). Detailed information is listed in Table 1. The observation has been applied in the diagnostic analysis of the air-sea interaction (Zhang et al., 2016; Yue et al., 2018).

3. Methods

The localized MS-EVA developed by Liang and Robinson (Liang, 2016; Liang and Anderson, 2007; Liang and Robinson, 2005, 2007) is used to explore the multiscale variability of eddy energetics in the SCS. This diagnostic analysis method has proven to be effective in the quantitative analysis of the interactions of multiscale scale processes in the ocean and atmosphere (Xu and Liang, 2020; Yang et al., 2017, 2020; Zhao & Liang, 2018, 2019; Zhao et al., 2016, 2019; Yang and Liang, 2019b). MS-EVA is based on a new functional analysis tool, namely, MWT developed by Liang and Anderson (2007). MWT can be viewed as a generalization of the classical Reynolds decomposition and was developed for a faithful reprentation of multiscale energy. It can decomposes a function space into a direct sum of orthogonal subspaces in the frequency domain, each with an exclusive range of scales while having the local (i.e., time-dependent) information retained. Liang and Anderson (2007) established that, for some specially constructed orthogonal filters, there exists a transfer–reconstruction pair, namely MWT and its counterpart multiscale window reconstruction (MWR). MWR functions like a filter in the traditional sense. What makes it different is that, for each MWR, there exists a corresponding MWT that gives coefficients which can be used to represent the time-dependent energy of the filtered series. Note that attempting to evaluate multiscale energy with filtered variable is con-ceptually wrong (see the appendix in Yang and Liang 2019a for a demonstration). In this study, we use the MWT to decompose the original fields into three orthogonal windows:

$$\Phi = \Phi^0 + \Phi^1 + \Phi^2, \tag{1}$$

where the superscripts 0, 1 and 2 represent a low-frequency background flow, a mid-frequency flow influenced by the typhoons and a high-frequency process, respectively. Here, the low-frequency background flow processes mostly include mesoscale processes and Kuroshio movement. The mid-frequency flow processes are the near-inertial processes caused by typhoons and the high-frequency processes. In the passage of the typhoons, we do not consider the interactions between low- and high-frequency processes or near-inertial processes, because of the limitations in the spatial resolution of the flow dataset.

Within the MWT framework, the KE and available potential energy (APE) in each window ϖ are

$$K^{\varpi} = \frac{1}{2}\widehat{u}_H^{\sim\varpi} \cdot \widehat{u}_H^{\sim\varpi} \tag{2}$$

and

$$A^{\varpi} = \frac{g^2}{2\rho_0 N^2}\left(\widehat{\rho}^{\sim\varpi}\right)^2, \tag{3}$$

where $N = \sqrt{-\frac{g}{f}\frac{d\rho}{dz}}$ is the buoyancy frequency, ρ and ρ_0 are the density and the reference density, g is the acceleration due to gravity, u_H is the two-dimensional horizontal velocity vector and $\sim\varpi$ denotes the variable on the window ϖ. Referring to the detailed derivation (Liang, 2016), the summarized time evolution of KE (K^{ϖ}) and APE (A^{ϖ}) are as follows:

$$\frac{\partial K^{\varpi}}{\partial t} = -\nabla \bullet Q_K^{\varpi} + \Gamma_K^{\varpi} - \nabla \bullet Q_P^{\varpi} + b^{\varpi} + F_K^{\varpi} \tag{4}$$

and

$$\frac{\partial A^{\varpi}}{\partial t} = -\nabla \bullet Q_A^{\varpi} + \Gamma_A^{\varpi} - b^{\varpi} + S_A^{\varpi} + F_A^{\varpi}, \tag{5}$$

where $-\nabla \bullet Q_K^{\varpi}$ (hereinafter ΔQ_K^{ϖ}) and $-\nabla \bullet Q_A^{\varpi}$ (hereinafter ΔQ_A^{ϖ}) are the convergence of the flux of KE and APE on window ϖ, respectively; Γ_K^{ϖ} and Γ_A^{ϖ} are the transfer of the KE and APE on window ϖ; $b^{\varpi} = -\frac{\rho}{\rho_0}\widehat{\rho}^{\sim\varpi}\widehat{w}^{\sim\varpi}$ is the buoyancy conversion on window ϖ to connect KE and APE; $-\nabla \bullet Q_P^{\varpi}$ (hereinafter ΔQ_P^{ϖ}) is the pressure flux convergence; S_A^{ϖ} is the source/sink of A^{ϖ} and can be ignored; F_K^{ϖ} and F_A^{ϖ} are the residual terms from the external forcings. Different from other energetics formalisms that appear in literature, the cross-scale transfer terms, i.e., Γ_K^{ϖ} and Γ_A^{ϖ}, satisfy an important conversation law:

$$\sum_n \sum_{\varpi} \Gamma_n^{\varpi} = 0, \tag{6}$$

where $\sum_{\varpi}$ and $\sum_n$ are the summation over all the scale windows ϖ and sampling time steps n, respectively. [The subscript n is omitted in Eqs. (2)–(5) for simplicity]. This means that Γ_K^{ϖ} and Γ_A^{ϖ} only redistribute energy among scale windows, without generating or destroying energy a whole. This property, though simply to state, does not hold in classical energetics formalisms. To distinguish, Γ_K^{ϖ} and Γ_A^{ϖ} will be termed barotropic and baroclinic canonical transfers in this study.

In particular, we focus on the mid-frequency window ($\varpi = 1$) energetics associated with near-inertial processes during the typhoon, which are written as:

$$\frac{\partial K^1}{\partial t} = \Gamma_K^{0\to1} + \Gamma_K^{2\to1} - \nabla \bullet Q_K^1 - \nabla \bullet Q_P^1 + b^1 + F_K^1 \tag{7}$$

and

$$\frac{\partial A^1}{\partial t} = \Gamma_A^{0\to1} + \Gamma_A^{2\to1} - \nabla \bullet Q_A^1 - b^1 + S_A^1 + F_A^1. \tag{8}$$

For near-inertial processes ($\varpi = 1$), the canonical transfer of KE ($\Gamma_K^{0\to1}$ and $\Gamma_K^{2\to1}$) or APE ($\Gamma_A^{0\to1}$ and $\Gamma_A^{2\to1}$) comes from the background flow processes ($\varpi = 0$) and the small-scale processes ($\varpi = 2$). For instance, a positive $\Gamma_K^{0\to1}$ ($\Gamma_A^{0\to1}$) means a forward transfer from background KE (APE) due to barotropic (baroclinic) instabilities; a positive $\Gamma_K^{2\to1}$ ($\Gamma_A^{2\to1}$) represents an inverse cascade of KE (APE) from the high-frequency processes to mid-frequency processes. The four diagnostics provide new insights and the criteria for scale-scale interactions, leading to evaluating the relative importance of barotropic and baroclinic instabilities.

Fig. 2 shows the energy exchanges in processes between the low-frequency window and the mid-frequency window. The window-to-window interactions between different scales denote the superscripts (e.g., 0→1, 2→1). Furthermore, the rate of eddy wind work (EWW) is calculated by:

$$\mathrm{EWW} = \frac{1}{\rho_0}\widehat{\mathbf{v}}^{\sim1} \bullet \widehat{\boldsymbol{\tau}}^{\sim1}. \tag{9}$$

Where $\mathbf{v}$ is the surface velocity and $\boldsymbol{\tau}$ is the surface wind stress. The superscript 1 denotes the mid-frequency window.

In previous work, typhoon-induced near-inertial oscillations have been considered as ubiquitous components of the oceanic energy budget. The period of near-inertial oscillations in our study region east of Taiwan (Fig. 1) is about 1.6 days. The cutoff period of window 1 is therefore taken as 0.5–2 days (= 3×2^3 to 3×2^4 h, where $dt = 3$ h is the temporal resolution of the HYCOM input data). We also tested other schemes (0.5–1 days, 0.5–4 days and 1–2 days) and the result were inferior to that we chose. The scale should to be chosen as a power of 2 (Liang, 2016).

In summary, the original fields are decomposed as three-scale windows: A low-frequency background window (of periods longer than two days), a mid-frequency window (of periods between 0.5 and 2 days), and a high-frequency window (of periods shorter than 0.5 day). The whole time series of data is 32 days (= 3×2^8 h), including the whole process of the typhoon. Table 2 lists the detailed parameters for the MS-EVA.

4. Results: verification of MS-EVA for Typhoon Kalmaegi

4.1. Results and validity

The temporal sampling rates of HYCOM and observation datasets are 12 min and 3 h, respectively. The power spectra of components of the velocity at 14 m for observations and HYCOM reanalysis datasets at P1

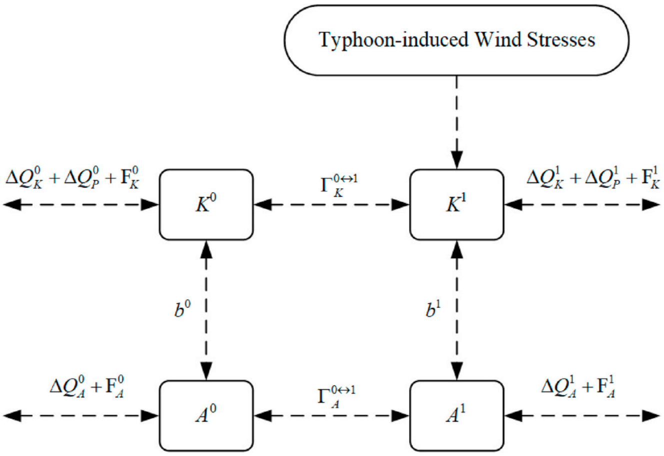

Fig. 2. Schematic diagram of the energy exchanges in the three-scale processes. We mainly focus on the processes indicated by the superscripts 0 and 1. The other energy transfers associated with the processes indicated by the superscript 2 are ignored.

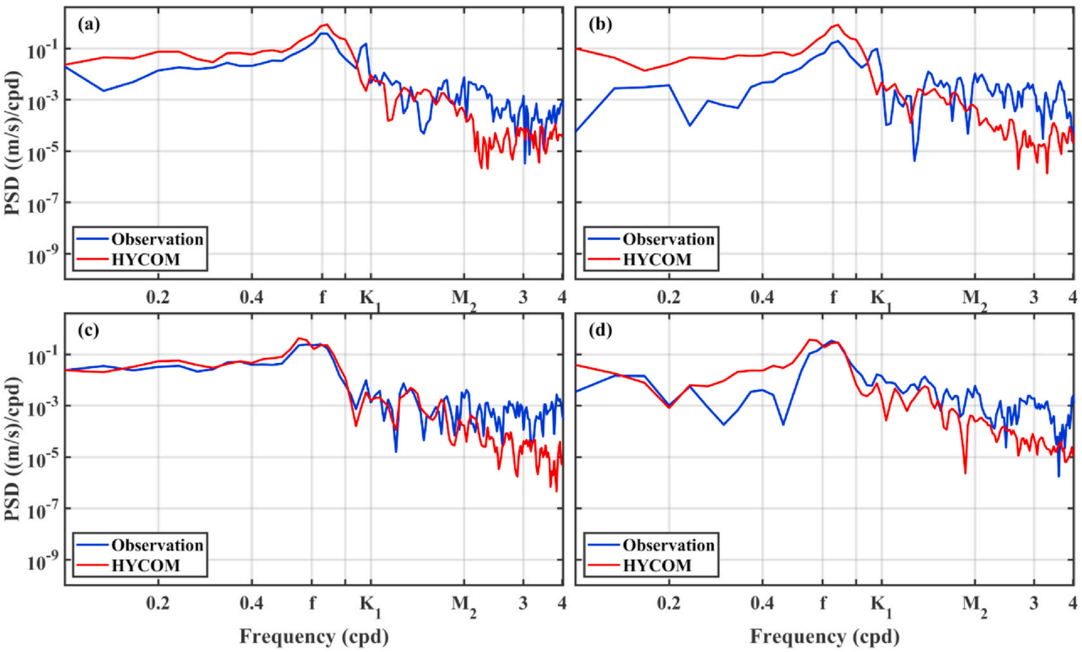

Fig. 3. Power spectra of components of the velocity at 14 m for observations (red) and HYCOM reanalysis data (blue) at P1 (a and b are the u and v components, respectively) on the left side of the track and at P2 (c and d are the u and v components, respectively) on the right side. The symbol f in the x-axis is the local inertial frequency field (see Section 4). The small kinetic energy (K^2) distributions mostly consist of high-frequency and other random signals (not shown).

Table 2
Detailed parameters in the MS-EVA.

Parameter	Value
Time	2014/09/01T00–2014/10/02T21
Scale level	$J_0 = 5$; $j_1 = 7$; $j_2 = 8$
Frequency window	Low-frequency: periods longer than two days
	Mid-frequency: periods between 0.5 and 2 days
	High-frequency: periods shorter than 0.5 day
Spatial range	115–128° E, 10–28° N
Grid	288 × 226
Vertical levels	40

and P2 illustrates that the dominant inertial processes (f in the x-axis) are well consistent during the typhoon, which demonstrates that HYCOM largely reproduces the feature observed in the SCS, as shown in previous studies about air-sea interaction in the period of the typhoon (He et al., 2022; Qiao et al., 2022; Quan et al., 2022). Compared with tidal signals, the near-inertial signals are more prominent during the typhoon. Tidal forces are not taken into account in HYCOM simulation, so the dominant frequency of inertial motions is well consistent in both datasets, which indicates that HYCOM has abilities to reveal the typhoon-induced oceanic responses and the underlying dynamics (see Fig. 3).

We reconstruct the variable fields into three windows using MS-EVA to examine the spatial distribution of the first two dynamical states. Fig. 4 gives Typhoon Kalmaegi (2014) as an example to verify the ability of MS-EVA to extract the states of the corresponding windows. The time mean and mean vertical integral of the low-frequency window K^0 capture well the background distribution of the Kuroshio system and some mesoscale eddy signals over the whole time period shown in Fig. 4a.

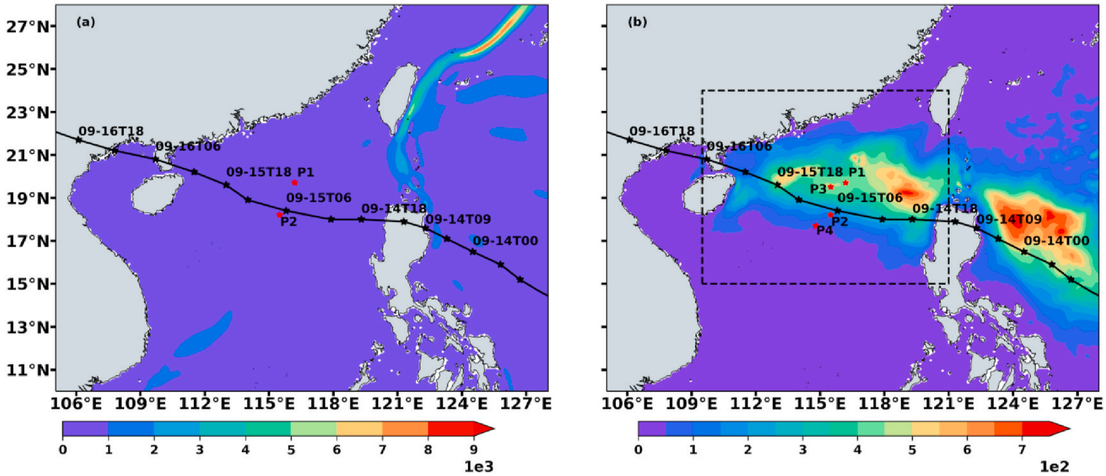

Fig. 4. Time mean distributions and vertical integral (upper 500 m) of kinetic energy (units: J m^{-2}) in the first two scale windows of the multiscale energy analysis for Typhoon Kalmaegi (2014): (a) low-frequency window K^0 and (b) mid-frequency window K^1. We mainly focus on the region surrounded with dashed lines in the K^1 window. The interval between each point in the tracks is 6 h. The two red stars P1 and P2 are the positions of the moorings and the other red stars P3 and P4 are used for dominant component analysis of the near-inertial energy.

Fig. 4b presents the typhoon-induced change in kinetic energy in the mid-frequency window during the passage of Typhoon Kalmaegi. Areas of high mean kinetic energy are located on the right-hand side of the storm track as a result of the strong interactions between the typhoon-induced wind stress and the current velocity in the mixed layer, consistent with previous studies (Chang et al., 2013; Yue et al., 2018). The region on the left-hand side shows abnormally large values caused by anticyclonic eddies in the background flow.

The current velocity and reconstructed velocity fields at P1 and P2 are plotted in Fig. 5a–f and 6a–6f for the whole time period. The most striking response of the ocean at both positions is a near-inertial oscillation in the upper ocean (Zhang et al., 2016). The near-inertial feature of the original current fields and the reconstructed velocity fields u^1 and v^1 maintain a high degree of consistency and the near-inertial current speed is up to 1 m s^{-1} during the period when the typhoon passes points P1 (Fig. 5a, c, 5d and 5f) and P2 (Fig. 6a, c, 6d and 6f), before decaying over a period of >10 days. The energy propagation plots show a downward trend because the typhoon-induced near-inertial internal waves transfer mechanical energy into the ocean interior (Fig. 5c, f, 6c and 6f). The near-inertial currents on the right-hand side of the track (P1; Fig. 5c and f) are stronger than those on the left-hand side (P2; Fig. 6c and f), which is the well-known “rightward bias”. The K^1 distribution of the kinetic energy shows a significant asymmetry between the two sides of the typhoon, suggesting that the near-inertial oscillations are intense (Cao et al., 2021). As a consequence, the near-inertial signals are extracted well via MS-EVA. The mid-frequency windows—namely, the near-inertial mode—can contribute to our understanding of the influence of typhoons on the upper ocean.

4.2. Dominant component analysis of the near-inertial energy

We use MS-EVA diagnostics to explore the multiscale energy analysis in the ocean and the interactions between different scales to determine the complex nonlinear dynamic processes occurring during the passage of Typhoons Kalmaegi. P1 and P2 are used to demonstrates that HYCOM reanalysis data largely reproduces the feature observed in the SCS during the typhoon. Instead of using P1 and P2 directly, the positions of P3 and P4 are more symmetrical relative to the typhoon track; the position of P2 is much closer to the main path. Therefore, we select additional points P3 and P4 as examples to compare the differences on either side of the typhoon track, based on the distance from the typhoon track and water depth (Fig. 4b).

Fig. 7a shows that the persistent period of the typhoon-induced near-inertial energy is about 5 day at point P3 (on the right-hand side of the typhoon track). The depth of influence of the near-inertial energy reaches up to 60 m below sea-level. By contrast, the near-inertial energy is extremely small compared with the energy on the right-hand side of the typhoon track (Fig. 7b). Fig. 8 depicts that the vertical distributions of the time evolution term of the kinetic energy $\partial K^1/\partial t$ at P3 (Fig. 8a) and P4 (Fig. 8b) are well matched with EWW variation (Fig. 8c and d), which is found that large (small) positive signals of EWW at P3 (P4) on the right (left) side of the typhoon track represents the strong (weak) energy fed from the local windLi et al., 2019; Liu et al., 2013. We also analyze the near-inertial energy budgets (Fig. 9a–g and 10a–10 g) in the upper ocean (upper 500 m) during the passage of Typhoon Kalmaegi and determine the K^1 budgets at points P3 and P4 over the whole time period. The influencing factors are the barotropic canonical transfer $\Gamma^{0\to1}$ and $\Gamma^{2\to1}$, the buoyancy conversion b^1, the horizontal kinetic energy transport $\Delta_h Q_K^1$, the vertical kinetic energy transport $\Delta_z Q_K^1$, the horizontal pressure work $\Delta_h Q_P^1$ and the vertical pressure work $\Delta_z Q_P^1$. These terms have either positive or negative feedbacks during Typhoon Kalmaegi.

After the typhoon passes point P3, the barotropic transfer $\Gamma^{0\to1}$ from the background window to the near-inertial window change from negative (up to -5.1×10^{-3} W m^{-3}) to positive (up to 2.7×10^{-3} W m^{-3}). The depth of influence of $\Gamma^{0\to1}$ is close to the depth of the influence of K^1 (Fig. 8a). This shows that the barotropic transfer during the typhoon has two stages: (1) $\Gamma^{0\to1}$ is negative for two to three days, indicating that KE is transferred from the near-inertial flow to the background flow; and (2) $\Gamma^{0\to1}$ is positive for about 4 days, indicating that KE is transferred from the background flow to the near-inertial flow via barotropic instabilities. The first stage mostly results from the wind stress (Chen et al., 2019) and the second has a link with the energy inverse cascade from the background mesoscale eddies to the near-inertial oscillations forced by the isotropic wind stress (Thomas, 2017). At point P4 (Fig. 10a), the values of $\Gamma^{0\to1}$ are weaker than at point P3. The magnitude of $\Gamma^{2\to1}$ at both P3 and P4 is almost negligible (Figs. 9b and 10b), which is limited by the resolution of HYCOM outputs.

The buoyancy conversion b^1 at point P3 has values of about $\pm 1.0 \times 10^{-3}$ W m^{-3} at depths of 50–150 m (Fig. 9c), and b^1 at point P4 has stronger signals in the ocean interior of upper 500 m (Fig. 10c). It shows that the energy pathways are different on either side of the typhoon

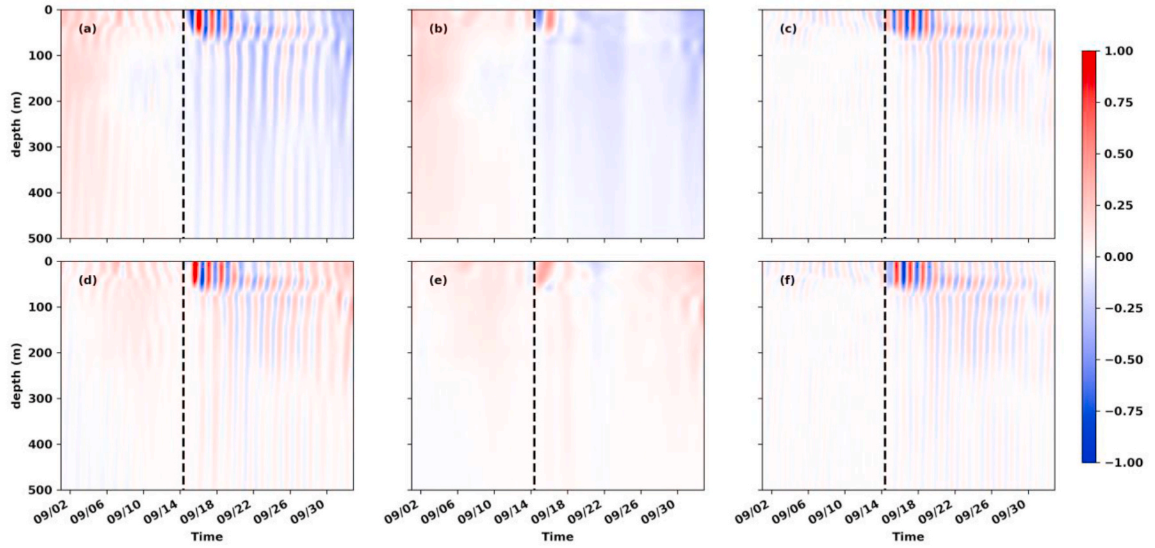

Fig. 5. Time series of the vertical distribution (units: m) of the single-point velocity components u and v (units: m s^{-1}) of Typhoon Kalmaegi in the upper ocean (500 m) at point P1. The each column of subgraphs is the original velocity (u: a and v: d) and two components (u^0: b, u^1: c; v^0: e, v^1: f) in the firt two of the multiscale transform windows for points P1, respectively. The dashed lines indicate the start time of the typhoon-induced effects on points P1.

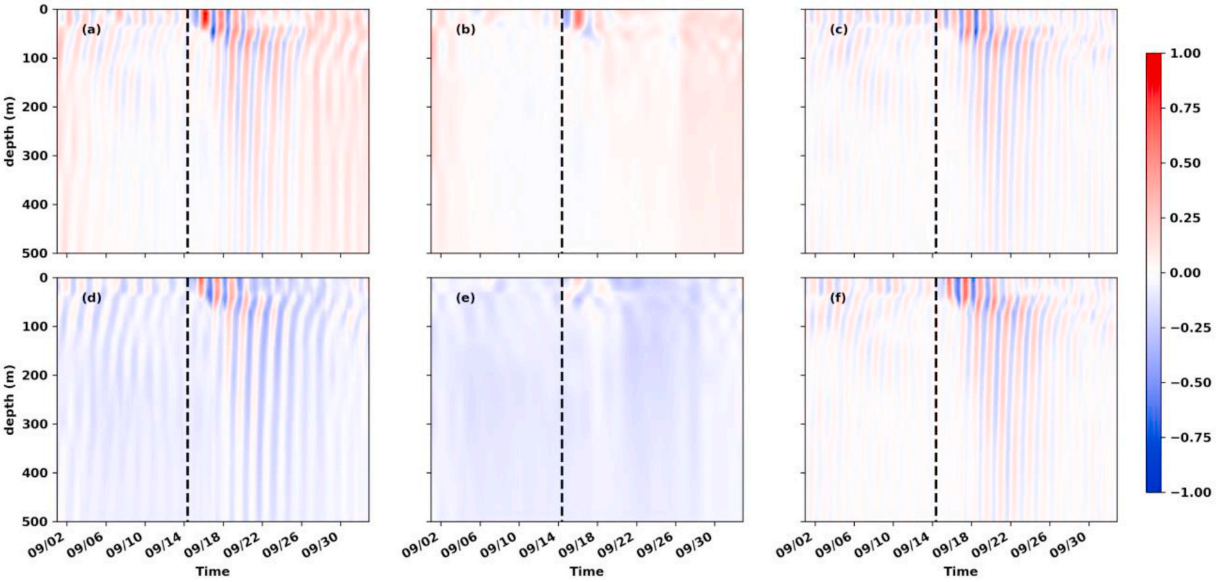

Fig. 6. Time series of the vertical distribution (units: m) of the single-point velocity components u and v (units: m s^{-1}) of Typhoon Kalmaegi in the upper ocean (500 m) at point P2. The each column of subgraphs is the original velocity (u: a and v: d) and two components (u^0: b, u^1: c; v^0: e, v^1: f) in the firt two of the multiscale transform windows for points P2, respectively. The dashed lines indicate the start time of the typhoon-induced effects on points P2.

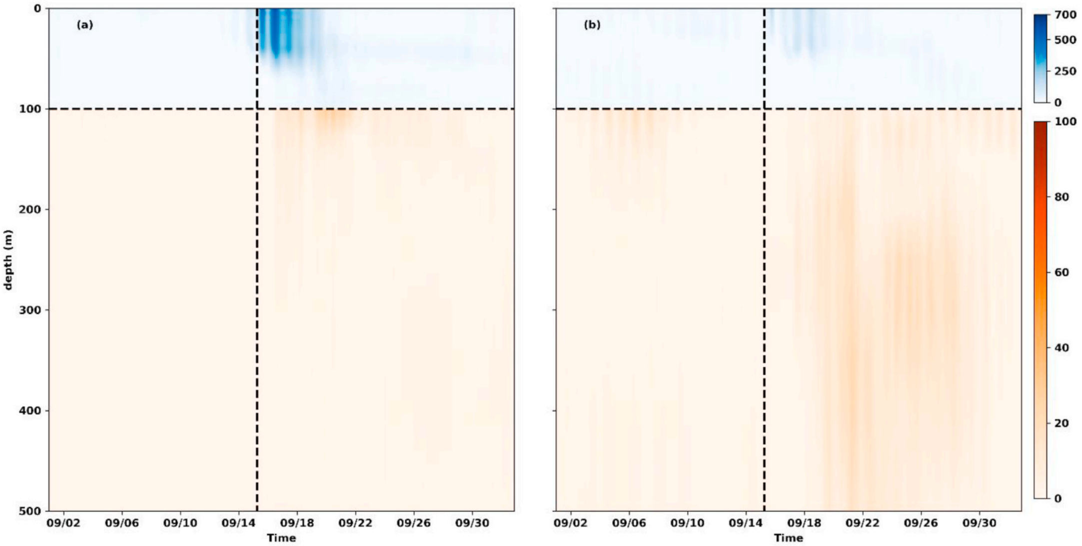

Fig. 7. Vertical distribution (units: m) of the kinetic energy K^1 (units: J m^{-3}) at the point P3 (a) and the point P4 (b). The dashed lines indicate the start time of typhoon-induced effects on points P3 and P4.

track. These results show one type of energy pathway associated with baroclinic instability for the conversion between near-inertial processes and mesoscale processes.

The divergence terms $\Delta_h Q_K^1$, $\Delta_z Q_K^1$, $\Delta_h Q_P^1$ and $\Delta_z Q_P^1$ in equation (4) represent non-local processes—namely, the horizontal and vertical advection and pressure work. The $\Delta_h Q_K^1$ at point P3 shows values of $\pm 2.5 \times 10^{-3}$ W m^{-3} at depths of 0–70 m (Fig. 9d). The $\Delta_z Q_K^1$ at point P3 varies at depths of 0–70 m (Fig. 9e). Advection redistributes the energy that transports KE to the right-hand side of the track, leading to upper ocean mixing. At point P4, $\partial K^1/\partial t$ goes through different stages: $\Delta_h Q_K^1$ and $\Delta_z Q_K^1$ vary at depths of 0–60 m (Fig. 10d and e), which are weaker than that at point P3. $\Delta_h Q_K^1$ and $\Delta_z Q_K^1$ on the left-hand side of the typhoon track therefore contribute to upper ocean mixing and enhances oceanic re-stratification.

The horizontal and vertical pressure work terms $\Delta_h Q_P^1$ and $\Delta_z Q_P^1$ have significantly different features that are up to two times larger than the other influencing factors. At point P3, $\Delta_h Q_P^1$ is negative during the first five days and then increases (Fig. 9f). This means that the pressure work first transfers near-inertial energy at depths of 0–100 m and then comes back because the transport of material is enhanced when the wind stress and typhoon move in the same direction. Fig. 9g shows that near-inertial energy is weakened in the upper layer of 0–75 m and is then strengthened in the deeper layer by the vertical pressure work. At point P4, $\Delta_h Q_P^1$ and $\Delta_z Q_P^1$ show no regularity in the upper ocean, because the directions of the wind and the typhoon movement are opposite. In all, the pressure work contributes to the redistributed of KE in the upper ocean, which strengthens the secondary circulation and enhances ocean mixing.

Fig. 11a illustrates that inverse energy cascade of KE ($K^1 \rightarrow K^0$), the divergence of KE ($\Delta Q_K^1 = \Delta_h Q_K^1 + \Delta_z Q_K^1$), and the pressure work ($\Delta Q_P^1 = \Delta_h Q_P^1 + \Delta_z Q_P^1$) are the major sink of near-inertial energy on the right side

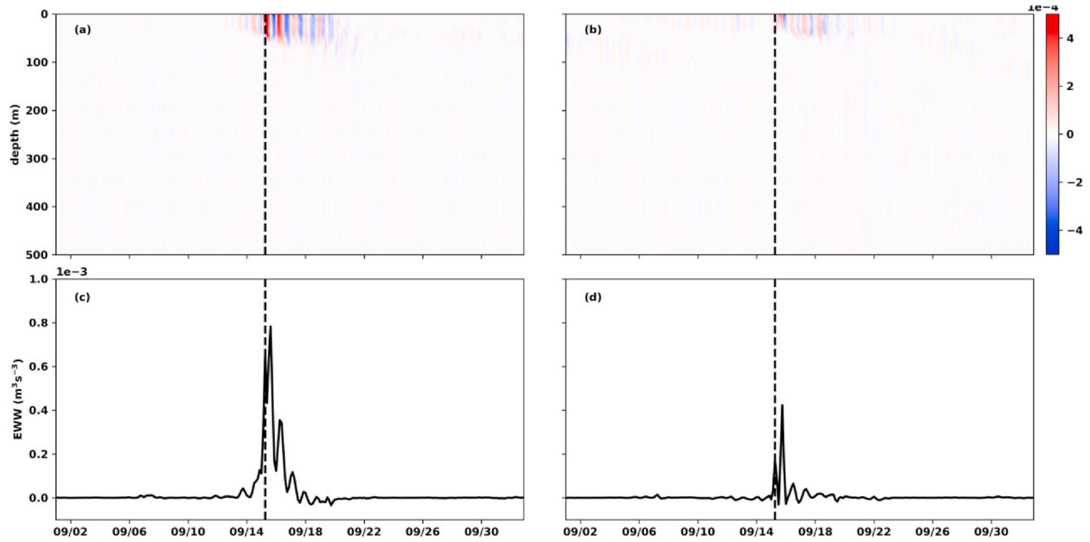

Fig. 8. Vertical distribution (units: m) of the time evolution term of the kinetic energy $\partial K^1/\partial t$ (units: W m^{-3}) and EWW (unit: m^3 s^{-3}) at point P3 (a and c) and point P4 (b and d). The dashed lines indicate the start time of typhoon-induced effects on points P3 and P4.

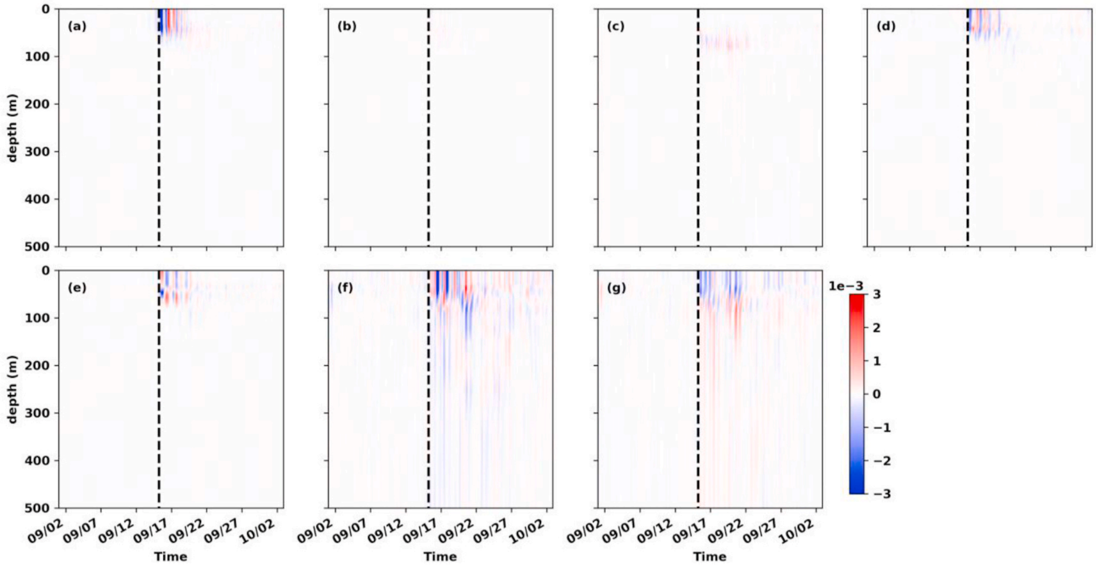

Fig. 9. Vertical distribution (units: m) of the transfer of K^1 energy for Typhoon Kalmaegi at point P3. (a) Transfer of barotropic instability from the background window to the near-inertial window $\Gamma^{0\to1}$. (b) Transfer of barotropic instability from the high-frequency window to the near-inertial window $\Gamma^{2\to1}$. (c) Buoyancy conversion rate term b^1. (d) Horizontal divergence term $\Delta_h Q_K^1$. (e) Vertical divergence term $\Delta_z Q_K^1$. (f) Horizontal pressure work term $\Delta_h Q_P^1$. (g) Vertical pressure work term $\Delta_z Q_P^1$ (units: W m^{-3}). The dashed lines indicate the starting time of the typhoon-induced effects at point P3.

of the typhoon track. The all terms are all weaker, expect for the pressure work (Fig. 11b).

These quantitative characteristics contribute to our understanding of the different processes on either side of Typhoon Kalmaegi. The fields reconstructed via MS-EVA capture the signals associated with the dynamical regimes of different windows. Determination of the near-inertial energy budget on either side of the typhoon provides quantitative information at points P3 and P4, which have similar features irrespective of the positions of the points on the two sides.

5. Multiscale impacts of vorticity on the response of the upper ocean to the typhoon

This section explores the characteristics of the multiscale impacts of vorticity on the typhoon-induced responses of the upper ocean. Previous work has shown that near-inertial oscillations passing downward are often related to modulation of the background current fields and positive (negative) vorticities, together with cyclonic (anticyclonic) eddies. Anticyclonic eddies favor the transfer of near-inertial energy into the interior of the ocean, whereas the opposite are observed for cyclonic eddies (Kawaguchi et al., 2020; Kunze, 1985; Leaman and Sanford, 1975). Fig. 12 shows that K^1 on the right-hand side of the typhoon track has regular varations: high (low) values of K^1 are accompanied by the strong (weak) relative vorticities, leading to stengthened (weakened) vertical mixing.

To investigate the inhomogeneous distribution of K^1 on the right-hand side of the typhoon track, we select two regions (A1 and A2) to compare the effects of positive and negative vorticities. Fig. 13b1 shows that the region A1 with a high K^1 benefits from negative vorticities. Fig. 14b1 shows that one anticyclonic eddy passed the region A1 and lasted about 6 days, leading to an intense downward propagation of the near-inertial energy. However, the region A2 mainly is controlled by

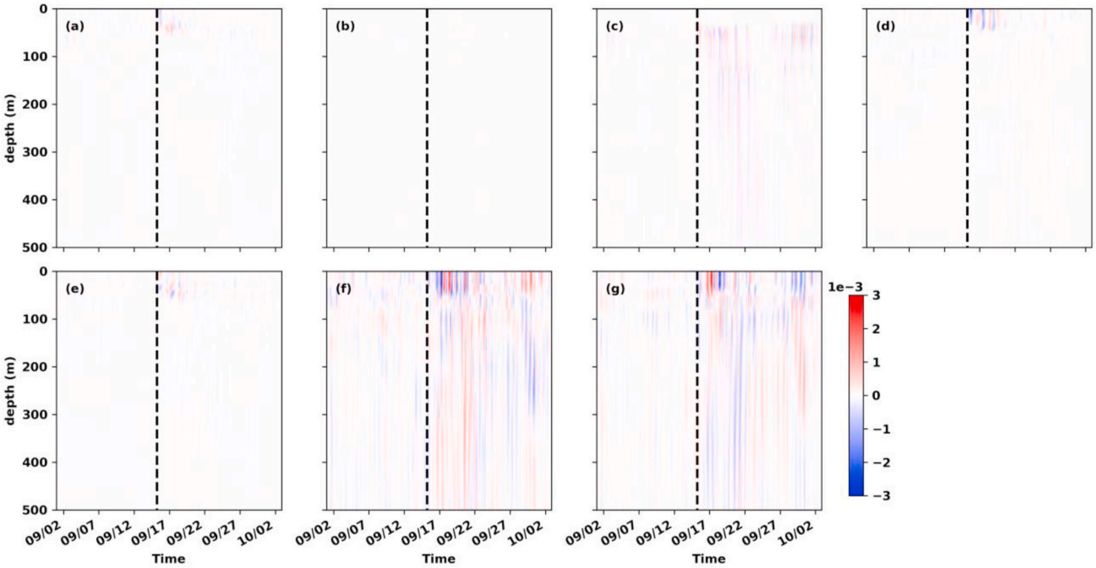

Fig. 10. Vertical distribution (units: m) of the transfer of K^1 energy for Typhoon Kalmaegi at point P4. (a) Transfer of barotropic instability from the background window to the near-inertial window $\Gamma^{0\to1}$. (b) Transfer of barotropic instability from the high-frequency window to the near-inertial window $\Gamma^{2\to1}$. (c) Buoyancy conversion rate term b^1. (d) Horizontal divergence term $\Delta_h Q_K^1$. (e) Vertical divergence term $\Delta_z Q_K^1$. (f) Horizontal pressure work term $\Delta_h Q_P^1$. (g) Vertical pressure work term $\Delta_z Q_P^1$ (units: W m^{-3}). The dashed lines indicate the starting time of the typhoon-induced effects at point P4.

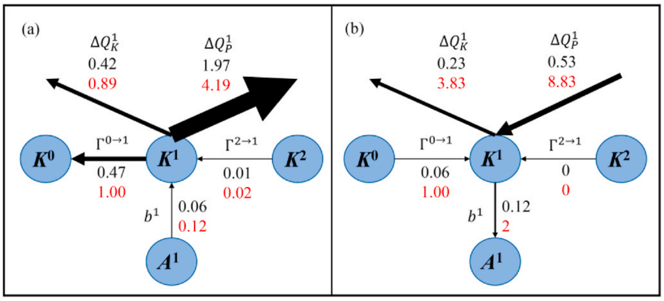

Fig. 11. Schematic energy pathways (vertical integration, unit: W m^{-2}) at P3 (a) and P4 (b). Each term has the absolute value of energy flow (black) and the ratio of $\Gamma^{0\to1}$ (red).

positive vorticity and thus results in weak K^1 (Fig. 14b2). The negative vorticity decreases in region A2 because the cyclonic eddy passes this region, temporarily blocking the downward propagation of the near-inertial energy (Fig. 13b2).

Taking into account into the effect of stratification and velocity shear, we use the Richardson number $R_i = \frac{N^2}{S^2} = \left(-\frac{g}{f}\frac{d\rho}{dz}\right) \Big/ \left(\left(\frac{\partial u}{\partial z}\right)^2 + \left(\frac{\partial v}{\partial z}\right)^2\right)$ to measure mixing in the upper ocean before and after the passage of the typhoon (Fig. 15). Ocean mixing in the region A1 increases at all depths of 0–500 m (Fig. 15a), which prevent the near-inertial energy reaching the ocean interior as a result of partial dissipation in the upper ocean (Fig. 13b1). In the region A2, ocean mixing in the upper 250 m shows no difference after the passage of the typhoon (Fig. 15b). Ocean mixing is clearly observed in region A2 at depths of 250–400 m. There is a general consensus in previous studies that the rightward bias results from asymmetrical

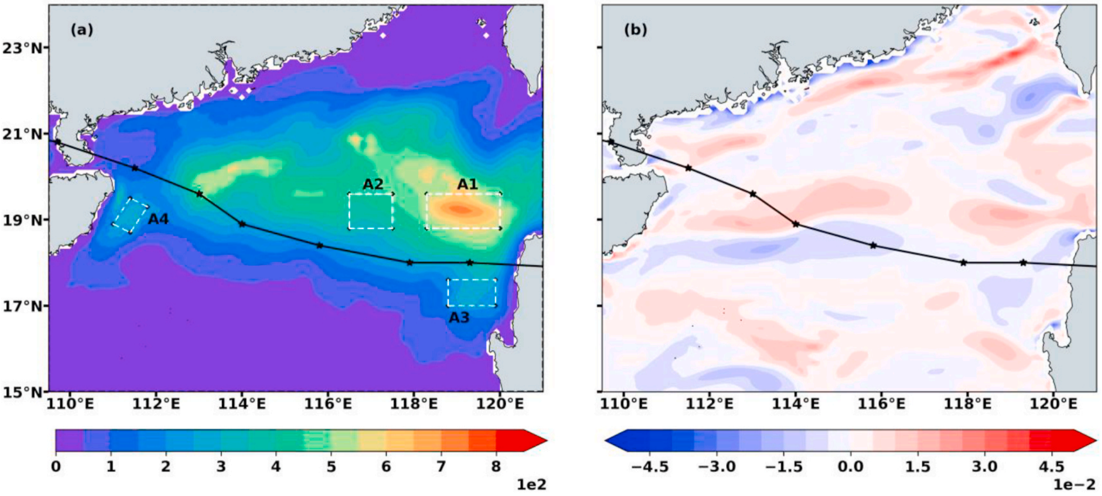

Fig. 12. (a) Time mean distributions and vertical integral (upper 500 m) of kinetic energy (units: J m^{-2}) in the first two scale windows. Regions A1 and A2 are used to analyze the effects of positive or negative vorticities on the right-hand side of the typhoon track, whereas regions A3 and A4 on left side of the track are used to analyze "leftward abnormal enhancement" of near-inertial energy. (b) Time mean distributions and vertical mean of relative vorticities (units: dimensionless) uring the typhoon passed the region.

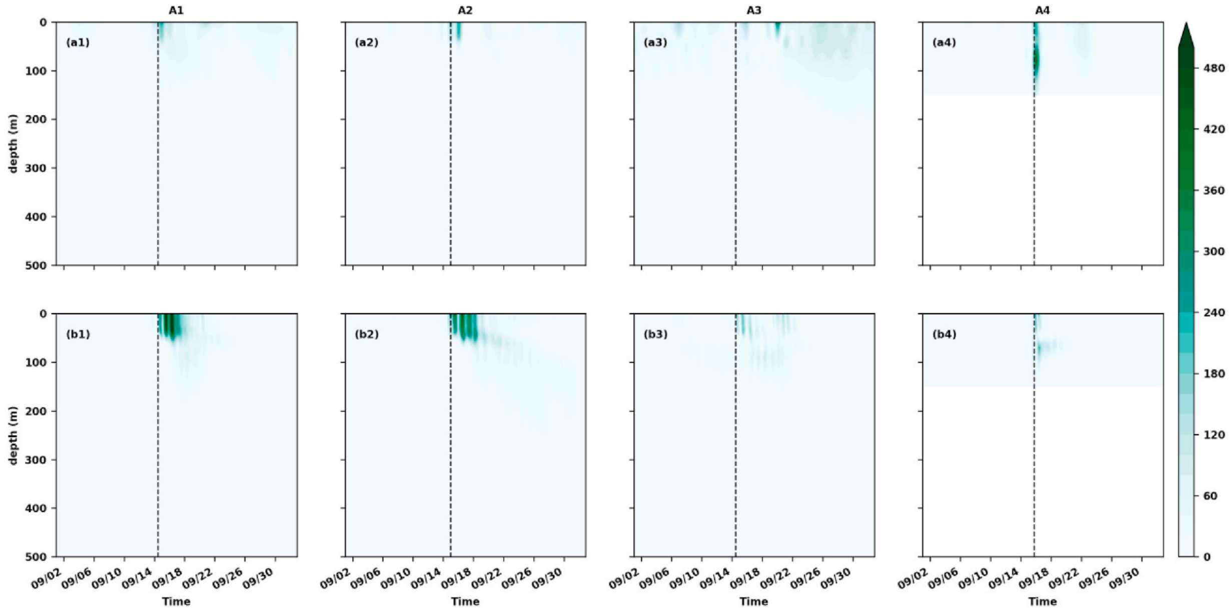

Fig. 13. Time series of the vertical distribution (units: m) of the regional average values of K^0 (a1–a4) and K^1 (b1–b4) in the different regions A1-A4 (units: J m^{-3}) The black dotted lines represent times that the typhoon has just begun to affect the region.

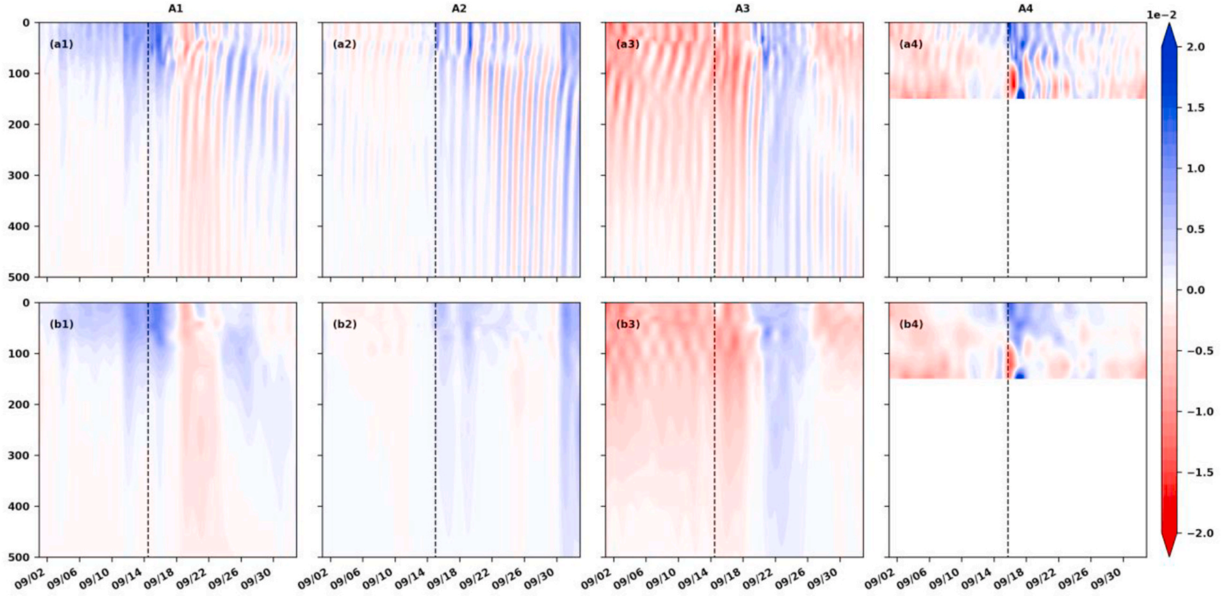

Fig. 14. Time series of the vertical distribution (units: m) of relative vorticity (units: imensionless): (a) the original velocity fields; (b) the reconstructed velocity fields $\mathbf{u}^0$. The numbers 1–4 represent the four regions A1-A4. The black dotted lines represent times that the typhoon has just begun to affect the region.

coupling between the wind stress and upper ocean on the right-hand side of the storm track (Liu et al., 2020; Yue et al., 2018). However, K^1 in the regions A3 and A4 are larger on the left-hand side than the other regions on the left-hand side in region (Fig. 12), in contrast to previous research. Ocean mixing in the regions A3 is relatively stronger at 250–300 m (Fig. 15c). And ocean mixing in the regions A4 is overall strengthened due to the shallow terrain (Fig. 15d).

We determine the regional average of the influencing terms of $\Gamma^{0\to1}$, $\Gamma^{2\to1}$, b^1, $\Delta_h Q_K^1$, $\Delta_z Q_K^1$, $\Delta_h Q_P^1$ and $\Delta_z Q_P^1$ to quantify the contribution of the near-inertial energy budgets in the upper 500 m of the ocean for different vorticities (Fig. 16). $\Gamma^{0\to1}$, $\Gamma^{2\to1}$ and b^1 have similar values. For the region A1, $\Delta_z Q_P^1$ is the main term for exchanging energy between the upper and deep ocean (Fig. 16g1), indicating that the pressure work transports near-inertial energy to deep ocean. At the regional A2, $\Delta_h Q_K^1$ and $\Delta_z Q_P^1$ make the near-inertial energy decrease and leads to weak ocean mixing in the upper 100 m (Fig. 16d2 and 16g2), whereas $\Delta_h Q_P^1$ contributes to near-inertial energy and leads to strong ocean mixing in the upper 150–300 m (Fig. 16f2). For the region A3 influenced by negative vorticities for about 3 days (Fig. 14b3), $\Delta_z Q_P^1$ is the dominate term for near-inertial energy increase. In the shallow terrain, pressure work greatly domainates the regional A4 (Fig. 16f4 and 16g4), although there are some positive vorticities (Fig. 14b4). These results help us to better understand the inhomogeneity of typhoon-induced inertial energy under the effect of vorticity.

6. Summary

We use a HYCOM simulation output to investigate the multiscale

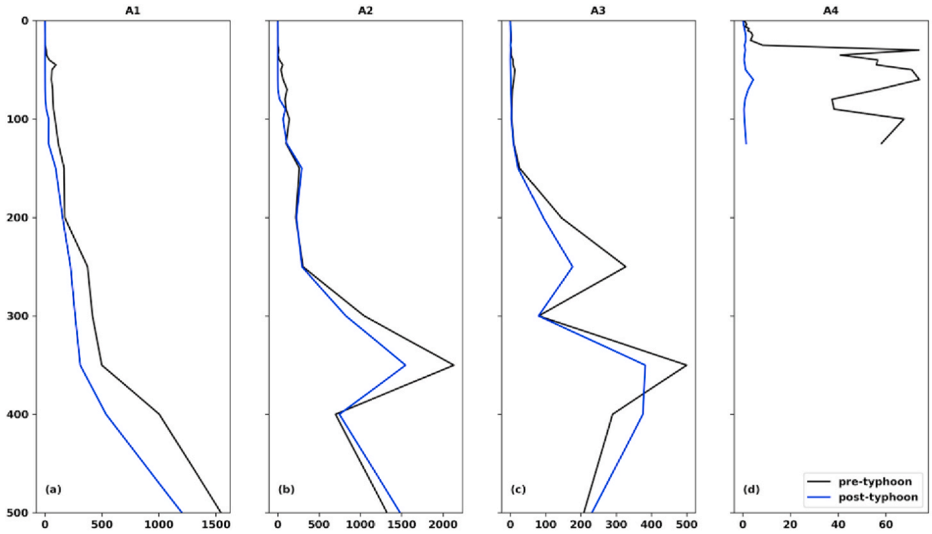

Fig. 15. Vertical distribution of the Richardson number (dimensionless) before (black lines) and after (blue lines) the passage of the typhoon. The symbols a-d represent the four regions A1-A4.

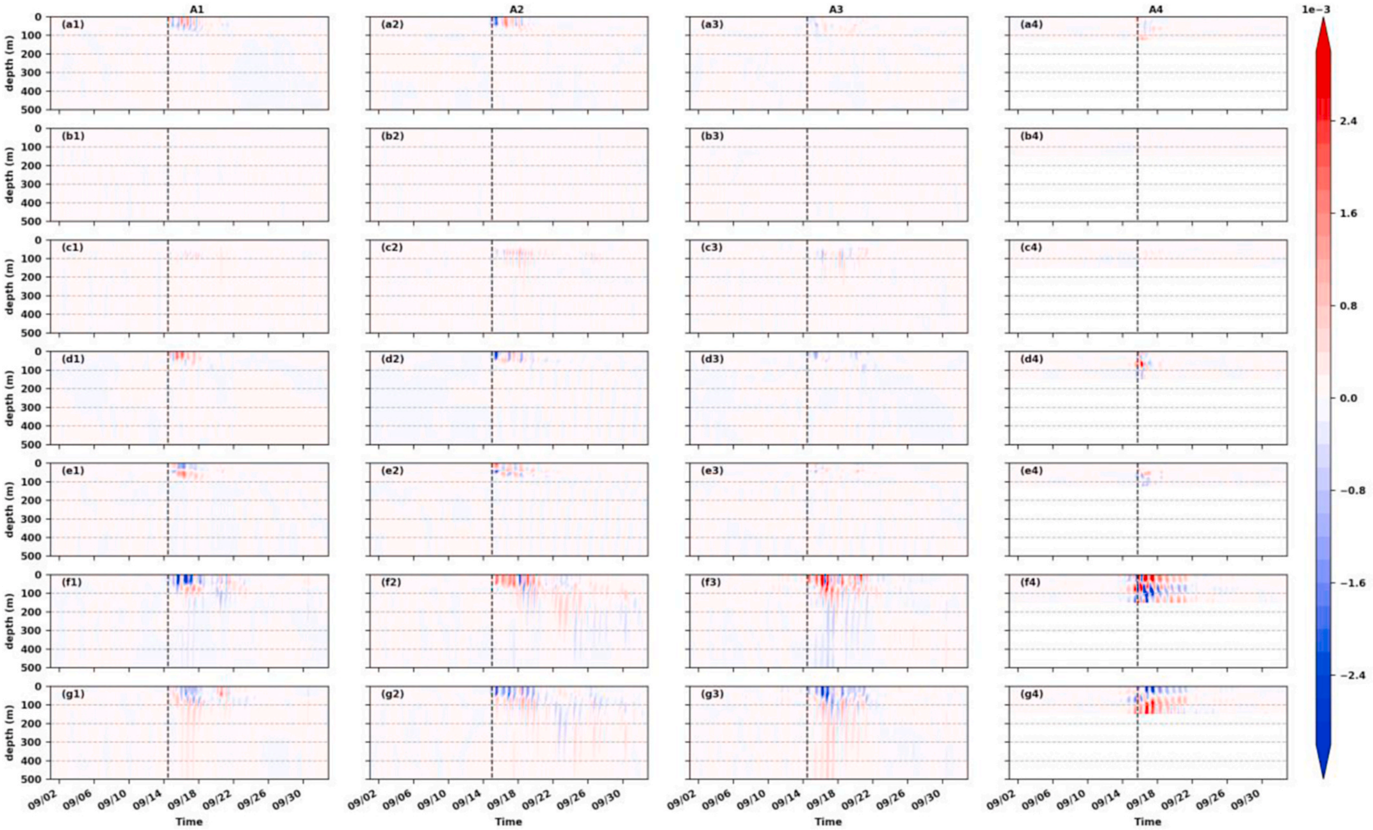

Fig. 16. Time series of the vertical distribution (units: m) of the regional average values of (a) $\Gamma^{0\to1}$, (b) $\Gamma^{2\to1}$, (c) b^1, (d) $\Delta_h Q_K^1$, (e) $\Delta_z Q_K^1$, (f) $\Delta_h Q_P^1$ and (g) $\Delta_z Q_P^1$ (units: W m^{-3}). The numbers 1–4 represent the four regions in Fig. 11a. The black dotted lines represent times that the typhoon has just begun to affect the region.

energy interactions of Typhoon Kalmaegi (2014) in the SCS. A three-scale energetics framework is used to analyze the multiscale typhoon-induced interactions; respectively, the low-frequency background flow, the mid-frequency flow influenced by the typhoon, and the high-frequency flow. By applying MS-EVA, we find that the background flow window represents mesoscale processes and Kuroshio currents, whereas the high-frequency window includes small-scale processes in the ocean. The mid-frequency flow window captures the typhoon-induced near-inertial energy characterized by a rightward bias, consistent with previous studies. The distribution of the near-inertial energy on the right-hand side of Typhoon Kalmaegi is heterogeneous due to the presence of both positive and negative vorticities. Negative vorticity contributes to the downward propagation of the near-inertial energy. MS-EVA provides a good method of investigating the spatiotemporal variability of multiscale interactions in the ocean during the passage of a typhoon.

The influencing terms are the barotropic canonical transfer $\Gamma^{0\to1}$, buoyancy conversion b^1, the horizontal transport of kinetic energy $\Delta_h Q_K^1$, the vertical transport of kinetic energy $\Delta_z Q_K^1$, horizontal pressure work $\Delta_h Q_P^1$ and vertical pressure work $\Delta_z Q_P^1$. We ignore $\Gamma^{2\to1}$ which is limited by the resolution of the HYCOM output. During the typhoon, the kinetic energy transfers from the near-inertial window to the background window, mainly on the right-hand side of the typhoon track, where the magnitude of the interactions is larger than that on the left-hand side. Advection redistributed energy, transporting and redistributing kinetic energy downwards from the surface of the ocean. The pressure work is stronger than the advection work, which contributes to the accumulation of kinetic energy in the ocean interior, leading to strengthening of the secondary circulation and enhancing ocean mixing.

Previous studies have shown that negative vorticity favors an increase in the downward propagation of the near-inertial energy and it is therefore desirable to determine the effect of vorticity. A negative vorticity significantly affects the distribution and downward propagation of the near-inertial energy, leading to heterogeneity in upper ocean mixing. Negative vorticity and pressure work partially result in "leftward abnormal enhancement", which is smaller than the increase in the near-inertial energy as a result of wind stress. The pressure work and negative vorticity increases the near-inertial energy in the upper 500 m of the ocean.

Although the typhoon-induced near-inertial energy has been studied previously, our analysis of the three orthogonal windows decomposed from the time series of the original variable fields via MS-EVA explains the multiscale interactions between mesoscale and near-inertial processes. The interactions between the near-inertial and sub-mesoscale process are limited by the coarse resolution of the HYCOM output and these mechanisms require further study using high-resolution ~1 km simulations.

Declaration of competing interest

The authors declare that they have no known competing financial interests or personal relationships that could have appeared to influence the work reported in this paper.

Data availability

The data that has been used is confidential.

Acknowledgements

This work was supported by the National Natural Science Foundation of China under Grants 42027805, 41620104003, and 42276017, Postgraduate Research & Practice Innovation Program of Jiangsu Province, grant numbers KYCX21_0959 and SJKY19_0968. Support is also acknowledged from the Canadian Ocean Frontier Institute, Canadian Space Agency's GRIP, Marine Environmental Observation Prediction and Response (MEOPAR), the Canada-Surface Water and Ocean Topography mission (C-SWOT), and the Canadian Aquatic Climate Change Adaptation Services Program. We acknowledge the High Performance Computing Center of Nanjing University of Information Science & Technology for their support of this work. Thanks to Huimin Li for proofreading the manuscript.

References

Cao, A., Guo, Z., Pan, Y., Song, J., He, H., Li, P., 2021. Near-inertial waves induced by typhoon megi (2010) in the South China sea. J. Mar. Sci. Eng. 9 (4), 440. https://doi.org/10.3390/jmse9040440.

Chai, X., Wang, L., 2019. A multiscale energetic diagnosis of the response of Mokpo sea to typhoon bolaven. J. Geosci. Environ. Protect. 7, 251. https://doi.org/10.4236/gep.2019.78019, 08.

Chang, Y.C., Chen, G.Y., Tseng, R.S., Centurioni, L.R., Chu, P.C., 2013. Observed near-surface flows under all tropical cyclone intensity levels using drifters in the northwestern Pacific. J. Geophys. Res.: Oceans 118 (5), 2367–2377. https://doi.org/10.1002/jgrc.20187.

Chen, Y., Chen, L., Zhang, H., Gong, W., 2019. Effects of wave-current interaction on the pearl river estuary during typhoon hato. Estuarine. Coast. Shelf Sci. 228, 106364 https://doi.org/10.1016/j.ecss.2019.106364.

Fu, L.L., Chelton, D.B., Le Traon, P.Y., Morrow, R., 2010. Eddy dynamics from satellite altimetry. Oceanography 23 (4), 14–25. https://doi.org/10.5670/oceanog.2010.02.

He, Y., Hu, P., Yang, Yin Y., Hou, Y., 2022. Volume transport in the East Taiwan Channel in response to different tracks of typhoons as revealed by HYCOM data. J. Oceanol. Limnol. 40, 22–36. https://doi.org/10.1007/s00343-021-0318-4.

Jin, W., Liang, C., Hu, J., Meng, Q., Lü, H., Wang, Y., et al., 2020. Modulation effect of mesoscale eddies on sequential typhoon-induced oceanic responses in the South China sea. Rem. Sens. 12 (18), 3059. https://doi.org/10.3390/rs12183059.

Kawaguchi, Y., Wagawa, T., Igeta, Y., 2020. Near-inertial internal waves and multiple-inertial oscillations trapped by negative vorticity anomaly in the central Sea of Japan. Prog. Oceanogr. 181, 102240 https://doi.org/10.1016/j.pocean.2019.102240.

Kunze, E., 1985. Near-inertial wave propagation in geostrophic shear. J. Phys. Oceanogr. 15 (5), 544–565. https://doi.org/10.1175/1520-0485(1985)015<0544:NIWPIG>2.0.CO;2.

Leaman, K.D., Sanford, T.B., 1975. Vertical energy propagation of inertial waves: a vector spectral analysis of velocity profiles. J. Geophys. Res. 80 (15), 1975–1978. https://doi.org/10.1029/JC080i015p01975.

Leipper, D.F., Volgenau, D., 1972. Hurricane heat potential of the Gulf of Mexico. J. Phys. Oceanogr. 2 (3), 218–224. https://doi.org/10.1175/1520-0485(1972)002<0218:HHPOTG>2.0.CO, 2.

Li, J., Xu, J., Liu, J., He, Y., Chen, Z., Cai, S., 2019. Correlation of near-inertial wind stress in typhoon and typhoon-induced oceanic near-inertial kinetic energy in the upper South China Sea. Atmosphere 10 (7), 388. https://doi.org/10.3390/atmos10070388.

Liang, X.S., 2016. Canonical transfer and multiscale energetics for primitive and quasigeostrophic atmospheres. J. Atmos. Sci. 73 (11), 4439–4468. https://doi.org/10.1175/JAS-D-16-0131.1.

Liang, X.S., Anderson, D.G., 2007. Multiscale window transform. Multiscale Model. Simul. 6 (2), 437–467. https://doi.org/10.1137/06066895X.

Liang, X.S., Robinson, A.R., 2005. Localized multiscale energy and vorticity analysis: I. Fundamentals. Dynam. Atmos. Oceans 38 (3–4), 195–230. https://doi.org/10.1016/j.dynatmoce.2004.12.004.

Liang, X.S., Robinson, A.R., 2007. Localized multi-scale energy and vorticity analysis: II. Finite-amplitude instability theory and validation. Dynam. Atmos. Oceans 44 (2), 51–76. https://doi.org/10.1016/j.dynatmoce.2007.04.001.

Lin, I., Liu, W.T., Wu, C.C., Wong, G.T.F., Hu, C., Chen, Z., et al., 2003. New evidence for enhanced ocean primary production triggered by tropical cyclone. Geophys. Res. Lett. 30 (13) https://doi.org/10.1029/2003GL017141.

Lin, I.I., Wu, C.C., Pun, I.F., Ko, D.S., 2008. Upper-ocean thermal structure and the western North Pacific category 5 typhoons. Part I: ocean features and the category 5 typhoons' intensification. Mon. Weather Rev. 136 (9), 3288–3306. https://doi.org/10.1175/2008MWR2277.1.

Liu, F., Tang, S., 2018. Influence of the interaction between typhoons and oceanic mesoscale eddies on phytoplankton blooms. J. Geophys. Res.: Oceans 123 (4), 2785–2794. https://doi.org/10.1029/2017JC013225.

Liu, F., Zhang, H., Ming, J., Zheng, J., Tian, D., Chen, D., 2020. Importance of precipitation on the upper ocean salinity response to typhoon kalmaegi (2014). Water 12 (2), 614. https://doi.org/10.3390/w12020614.

Liu, L., Fei, J., Cheng, X., Huang, X., 2013. Effect of wind-current interaction on ocean response during Typhoon KAEMI (2006). Sci. China Earth Sci. 56 (3), 418–433. https://doi.org/10.1007/s11430-012-4548-3.

Morrow, R., Le Traon, P.Y., 2012. Recent advances in observing mesoscale ocean dynamics with satellite altimetry. Adv. Space Res. 50 (8), 1062–1076. https://doi.org/10.1016/j.asr.2011.09.033.

Pan, G., Chai, F., Tang, D., Wang, D., 2017. Marine phytoplankton biomass responses to typhoon events in the South China Sea based on physical-biogeochemical model. Ecol. Model. 356, 38–47. https://doi.org/10.1016/j.ecolmodel.2017.04.013.

Pan, J., Huang, L., Devlin, A.T., Lin, H., 2018. Quantification of typhoon-induced phytoplankton blooms using satellite multi-sensor data. Rem. Sens. 10 (2), 318. https://doi.org/10.3390/rs10020318.

Qiao, M., Cao, A., Song, J., Pan, Y., He, H., 2022. Enhanced turbulent mixing in the upper ocean induced by super typhoon goni (2015). Rem. Sens. 14 (10), 2300. https://doi.org/10.3390/rs14102300.

Quan, Q., Liu, Z., Yang, Y., Cai, Z., Zhang, H., Liu, X., 2022. Characterization of intraseasonal fluctuations in the abyssal South China Sea: an insight into the energy pathway. Prog. Oceanogr. 206, 102829 https://doi.org/10.1016/j.pocean.2022.102829.

Shan, H., Guan, Y., Huang, J., 2014. Investigating different bio-responses of the upper ocean to Typhoon Haitang using Argo and satellite data. Chin. Sci. Bull. 59 (8), 785–794. https://doi.org/10.1007/s11434-013-0101-9.

Shang, S., Li, L., Sun, F., Wu, J., Hu, C., Chen, D., et al., 2008. Changes of temperature and bio-optical properties in the South China Sea in response to Typhoon Lingling, 2001. Geophys. Res. Lett. 35 (10) https://doi.org/10.1029/2008GL033502.

Sun, L., Yang, Y.J., Xian, T., Lu, Z.M., Fu, Y.F., 2010. Strong enhancement of chlorophyll a concentration by a weak typhoon. Mar. Ecol. Prog. Ser. 404, 39–50. https://doi.org/10.3354/meps08477.

Thomas, L.N., 2017. On the modifications of near-inertial waves at fronts: implications for energy transfer across scales. Ocean Dynam. 67 (10), 1335–1350. https://doi.org/10.1007/s10236-017-1088-6.

Wang, S., Li, S., Hu, J., Geng, B., 2016. Experiments in optimizing simulations of the subsurface chlorophyll maximum in the South China Sea. J. Mar. Syst. 156, 1–15. https://doi.org/10.1016/j.jmarsys.2015.11.003.

Wu, R., Li, C., 2018. Upper ocean response to the passage of two sequential typhoons. Deep Sea Res. Oceanogr. Res. Pap. 132, 68–79. https://doi.org/10.1016/j.dsr.2017.12.006.

Xu, F., Liang, X.S., 2020. The synchronization between the zonal jet stream and temperature anomalies leads to an extremely freezing North America in January 2019. Geophys. Res. Lett. 47 (19), e2020GL089689 https://doi.org/10.1029/2020GL089689.

Yang, Y., Liang, X.S., 2018. On the seasonal eddy variability in the Kuroshio Extension. J. Phys. Oceanogr. 48 (8), 1675–1689. https://doi.org/10.1175/JPO-D-18-0058.1.

Yang, Y., Liang, X.S., 2019a. New perspectives on the generation and maintenance of the Kuroshio large meander. J. Phys. Oceanogr. 49 (8), 2095–2113. https://doi.org/10.1175/JPO-D-18-0276.1.

Yang, Y., Liang, X.S., 2019b. Spatiotemporal variability of the global ocean internal processes inferred from satellite observations. J. Phys. Oceanogr. 49 (8), 2147–2164. https://doi.org/10.1175/JPO-D-18-0273.1.

Yang, Y., Liang, X.S., Qiu, B., Chen, S., 2017. On the decadal variability of the eddy kinetic energy in the Kuroshio Extension. J. Phys. Oceanogr. 47 (5), 1169–1187. https://doi.org/10.1175/JPO-D-16-0201.1.

Yang, Y., Weisberg, R.H., Liu, Y., Liang, X.S., 2020. Instabilities and multiscale interactions underlying the loop current eddy shedding in the Gulf of Mexico. J. Phys. Oceanogr. 50 (5), 1289–1317. https://doi.org/10.1175/JPO-D-19-0202.1.

Yue, X., Zhang, B., Liu, G., Li, X., Zhang, H., He, Y., 2018. Upper ocean response to typhoon Kalmaegi and Sarika in the South China Sea from multiple-satellite observations and numerical simulations. Rem. Sens. 10 (2), 348. https://doi.org/10.3390/rs10020348.

Zhang, H., Chen, D., Zhou, L., Liu, X., Ding, T., Zhou, B., 2016. Upper ocean response to typhoon Kalmaegi (2014). J. Geophys. Res.: Oceans 121 (8), 6520–6535. https://doi.org/10.1002/2016JC012064.

Zhao, H., Han, G., Zhang, S., Wang, D., 2013. Two phytoplankton blooms near Luzon Strait generated by lingering Typhoon Parma. J. Geophys. Res.: Biogeosciences 118 (2), 412–421. https://doi.org/10.1002/jgrg.20041.

Zhao, H., Pan, J., Han, G., Devlin, A.T., Zhang, S., Hou, Y., 2017. Effect of a fast-moving tropical storm W ashi on phytoplankton in the northwestern S outh C hina S ea. J. Geophys. Res.: Oceans 122 (4), 3404–3416. https://doi.org/10.1002/2016JC012286.

Zhao, Y.B., Liang, X.S., 2019. Causes and underlying dynamic processes of the mid-winter suppression in the North Pacific storm track. Sci. China Earth Sci. 62 (5), 872–890. https://doi.org/10.1007/s11430-018-9310-5.

Zhao, Y.B., Liang, X.S., Gan, J., 2016. Nonlinear multiscale interactions and internal dynamics underlying a typical eddy-shedding event at L uzon S trait. J. Geophys. Res.: Oceans 121 (11), 8208–8229. https://doi.org/10.1002/2016JC012483.

Zhao, Y.B., Liang, X.S., Guan, Z., Hodges, K.I., 2019. The asymmetric eddy–background flow interaction in the North Pacific storm track. Q. J. R. Meteorol. Soc. 145 (719), 575–596. https://doi.org/10.1002/qj.3453.

Zhao, Y.B., Liang, X.S., 2018. On the inverse relationship between the boreal wintertime Pacific jet strength and storm-track intensity. J. Clim. 31 (23), 9545–9564. https://doi.org/10.1175/JCLI-D-18-0043.1.

Zheng, Z.W., Ho, C.R., Zheng, Q., Kuo, N.J., Lo, Y.T., 2010a. Satellite observation and model simulation of upper ocean biophysical response to Super Typhoon Nakri. Continent. Shelf Res. 30 (13), 1450–1457. https://doi.org/10.1016/j.csr.2010.05.005.

Zheng, Z.W., Ho, C.R., Zheng, Q., Lo, Y.T., Kuo, N.J., Gopalakrishnan, G., 2010b. Effects of preexisting cyclonic eddies on upper ocean responses to Category 5 typhoons in the western North Pacific. J. Geophys. Res.: Oceans 115 (C9). https://doi.org/10.1029/2009JC005562.